E×B Flux Driven Detachment Bifurcation in the DIII-D Tokamak

A. E. Jaervinen, S. L. Allen, D. Eldon, M. E. Fenstermacher, M. Groth, D. N. Hill, A. W. Leonard, A. G. McLean, G. D. Porter, T. D. Rognlien, C. M. Samuell, and H. Q. Wang

E × B Flux Driven Detachment Bifurcation in DIII-D

A.E. Jaervinen,* S.L. Allen, D. Eldon,† M.E. Fenstermacher, M. Groth,‡ D.N. Hill,† A.W.
Leonard,† A.G. McLean, G.D. Porter, T.D. Rognlien, C.M. Samuell, and H.Q. Wang§

Lawrence Livermore National Laboratory

(Dated: June 21, 2018)

A bifurcative step transition from low-density, high-temperature, attached divertor conditions to high-density, low-temperature, detached divertor conditions is experimentally observed in DIII-D tokamak plasmas as density is increased. The step transition is only observed in high confinement mode and only when the $\mathbf{B} \times \nabla B$-drift is directed towards the divertor. This work reports for the first time a theoretical explanation and numerical simulations that qualitatively reproduce this bifurcation and its dependence on toroidal field direction. According to the model, the bifurcation is primarily driven by the interdependence of the $\mathbf{E} \times \mathbf{B}$-drift fluxes, divertor electric potential structure, and divertor conditions. In attached conditions, strong potential gradients in the low field side (LFS) divertor drive $\mathbf{E} \times \mathbf{B}$-drift flux towards the high field side divertor, reinforcing low density, high temperature conditions in the LFS divertor leg. At the onset of detachment, reduction in the potential gradients in the LFS divertor leg reduce the $\mathbf{E} \times \mathbf{B}$-drift flux as well, such that the divertor plasma evolves non-linearly to high density, strongly detached conditions. Experimental estimates of the $\mathbf{E} \times \mathbf{B}$-drift fluxes, based on divertor Thomson scattering measurements, and their dependence on the divertor conditions are qualitatively consistent with the numerical predictions. The implications for divertor power exhaust and detachment control in the next step fusion devices are discussed.

PACS numbers: 52.55.Fa

The role of $\mathbf{E} \times \mathbf{B}$-drifts on bifurcation-like confinement transitions in toroidally confined fusion plasmas has been widely discussed in the scientific literature [1, 2, and references therein]. In this letter, we describe for the first time a bifurcation-like transition in divertor plasma conditions in the DIII-D tokamak driven by $\mathbf{E} \times \mathbf{B}$-drift fluxes. This type of bifurcation-like divertor plasma condition transitions have also been previously observed in the Joint European Torus (JET) fusion plasma device, while physics explanations of the phenomenon remained open [3].

Highly radiating boundary plasmas with cold, dissipative conditions in front of the divertor targets are presently favored as the primary divertor heat flux control solution for future fusion devices [4, 5]. These divertor plasma conditions, commonly called as *detached*, are routinely obtained in existing tokamaks by injecting fuel particles and radiating impurities into the plasma to reduce the divertor plasma electron temperature, T_e, down to below a few eV [5, and references therein]. At these temperatures, atomic physics processes become effective at mitigating plasma pressure, p, and reducing the conducted and recombination heat fluxes to the plate further than could be achieved solely by volumetric radiation [6]. The key parameter to be controlled when operating with detached divertor legs is the extent at which the upper end of the cold plasma region below $T_e \sim 5$ eV, i.e., the *detachment front*, is located in the divertor leg between the target and the X-point [7, 8] (Fig. 1). The front must be sufficiently far away from the target to provide enough leverage for the active control system to avoid transient re-attachment and overheating of the divertor materials

at all times. On the other hand, various degrees of degradation of core plasma properties have been observed in existing devices when the detachment front has reached the X-point [9–12, and references therein].
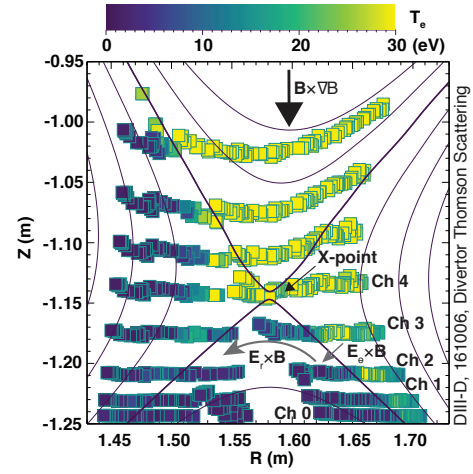

FIG. 1. 2D map of Divertor Thomson Scattering (DTS) measurements in DIII-D shots 161006 collected over an X-point sweep [13]. The channels 0 to 4 are labeled. The schematics of radial and poloidal $\mathbf{E} \times \mathbf{B}$-drift directions are illustrated with grey arrows. Low field side (LFS) and high field side (HFS) are also labeled on the figure.

In high confinement mode (H-mode) operation with the $\mathbf{B} \times \nabla B$-drift direction towards the active X-point in the DIII-D tokamak, the low field side (LFS) target plate is observed to undergo a rapid step transition from well attached conditions, $T_{e,\text{ target}} \sim 10 - 20$ eV,
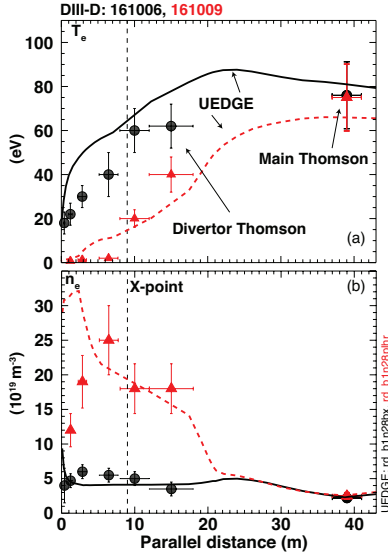
FIG. 2. Measured and simulated T_e (a) and n_e (b) profiles along a flux tube near the separatrix in the LFS SOL. Black circles represent DTS and main Thomson measurements in the attached LFS conditions. Black solid line represents UEDGE simulation in these conditions. The red triangles represent measurements in the detached LFS conditions, and the red dashed line a UEDGE simulation in detached conditions. The UEDGE simulations correspond to normalized poloidal flux, $\Psi_n \sim 1.0009$. The DTS data represents peak values within $\Psi_n \in [1.000, 1.004]$.

to strongly detached conditions, $T_{e,\,\text{target}} \sim 1$ eV with increasing plasma density (Fig. 1, 2, 3a, 4a) [14, 15]. Such step transitions would be a significant challenge for the detachment control systems in next step fusion devices. The high field side (HFS) divertor leg is detached in both conditions. UEDGE [16] simulations with cross-field drifts included do qualitatively reproduce the existence of these two divertor condition solutions (Fig. 2). For the same boundary conditions and upstream separatrix n_e, the simulations either converge to well attached solution with the LFS $T_{e,\,\text{target}}$ of 20 eV or well detached solution with $T_{e,\,\text{target}}$ of 1 eV, depending on the initial divertor conditions. If the simulations are started with high density, low temperature divertor conditions, the solver converges into the detached solution. On the other hand, starting the simulations with attached LFS divertor conditions, the solver converges into the attached solution. These simulations include carbon impurities with sputtering sources calculated according to published sputtering yields [17, 18].

In this letter, we show that the non-linear interaction of the divertor T_e and $\mathbf{E} \times \mathbf{B}$-drift driven particle fluxes can drive step like detachment transitions in the LFS divertor in H-mode, when the $\mathbf{B} \times \nabla B$-drift is directed towards the active X-point. In attached LFS conditions, $T_{e,\,\text{target}} \sim 10 - 20$ eV, the divertor electric potential structures lead to an $\mathbf{E} \times \mathbf{B}$-drift driven particle flux from

the LFS to HFS divertor, which reduces n_e and increases T_e in front of the LFS target for a given upstream $n_{e,\,\text{sep}}$ (Fig. 1). Using Divertor Thomson Scattering (DTS) [13] profiles to estimate the electric potential structure and $\mathbf{E} \times \mathbf{B}$-flows in the divertor leg, as was done in [19], we show that a particle flux of the order of 50% of the integrated LFS divertor target recycling flux enters into this $\mathbf{E} \times \mathbf{B}$-flow channel to the HFS divertor, consistent with previous reciprocating probe measurements in DIII-D [20]. As the upstream $n_{e,\,\text{sep}}$ is increased, $T_{e,\,\text{target}}$ is reduced. At the detachment threshold, the T_e reduction in front of the LFS plate reduces the electric potential gradients and the $\mathbf{E} \times \mathbf{B}$-drift driven particle sink in the LFS divertor. This increases n_e and radiated power in the LFS divertor leg, reducing T_e in front of the target further, driving the plasma to a strongly detached, high n_e, low T_e, and high carbon radiation conditions. The DTS measurement-based estimates show that the $\mathbf{E} \times \mathbf{B}$-flux from LFS to HFS is a factor of $3-5$ lower in detached than in attached conditions. These estimates are qualitatively consistent with predictions calculated with the 2D fluid code UEDGE and previous measurements [16, 20].

The focus in this letter is on a DIII-D H-mode density scan operated at a plasma current I_p of 0.9 MA and toroidal magnetic field of B_T of 1.8 T with 4 MW of neutral beam heating [21]. In these plasmas, the X-point is slowly swept across the DTS chords at major radius 1.49 m to obtain n_e and T_e measurements for both divertor legs (Figs. 1, 2). These plasmas were simulated with UEDGE including cross-field drifts (Fig. 2).

The poloidal electric field in the SOL [16, 22, 23] is given by

$$E_\theta = -\frac{\partial \Phi}{\partial \theta} = \frac{B_{\text{total}}}{B_\theta} \left(\frac{j_\parallel}{\sigma_\parallel} - \frac{0.71}{e}\frac{\partial T_e}{\partial s_\parallel} - \frac{1}{ne}\frac{\partial p_e}{\partial s_\parallel} \right). \quad (1)$$

The $j_\parallel$ current term is neglected, which is a good approximation in attached conditions. In detached conditions the current term can become important and will be discussed in this letter. For DIII-D shot 161006 with attached LFS conditions, the target Langmuir Probes measure parallel current, $j_\parallel$, in the common SOL of $1 - 1.5 \times 10^5$ A/m². The electrical conductivity in the SOL for T_e of $20 - 40$ eV is $\sigma_\parallel \sim 1 - 3 \times 10^5$ $\Omega^{-1}\text{m}^{-1}$. Therefore, the current term, $j_\parallel/\sigma_\parallel$, is estimated to be of the order of $0.5 - 1.5$ V/m. The thermoelectric term is estimated to be of the order of 2 V/m and the the pressure gradient term of the order of $3 - 4$ V/m, based on DTS measurements (Fig. 2).Therefore, neglecting the current term is estimated to modify the parallel potential gradient by less than 30% in attached LFS conditions. This analysis is supported by the UEDGE simulations.

Without the current term, equation 1 can be integrated to give the electric potential in the flux tube:

$$\Phi = \frac{0.71}{e}T_e + \frac{1}{ne}p_e + \Phi_{\text{sheath}} = \frac{1.71}{e}T_e + \Phi_{\text{sheath}}, \quad (2)$$

where Φ_{sheath} is the plasma potential at the sheath edge, for which the approximation $\Phi_{\text{sheath}} \approx 3T_{e,\text{ target}}/e$ is used. Therefore, an inferred plasma potential value is obtained for each Thomson scattering measurement point in the divertor. Next the integrated particle flux that is transported from the LFS divertor to HFS divertor is calculated:

$$\Gamma_{\mathbf{E}\times\mathbf{B} \text{ , PFR}} = 2\pi R \int_{-\infty}^{0} n(r)v_{\mathbf{E}\times\mathbf{B}}(r)dr, \qquad (3)$$

where $2\pi R$ represents the toroidal circumference and the radial integration propagates through the private flux region. Substituting $v_{\mathbf{E}\times\mathbf{B}}(r) = \frac{E(r)}{B_T} = -\frac{\partial\Phi}{B_T\partial r}$ and assuming that $n(r) = n_0 e^{-\frac{|r|}{\lambda_n}}$ and $\Phi(r) = \Phi_0 e^{-\frac{|r|}{\lambda_\Phi}}$, equation 3 can be solved:

$$\Gamma_{\mathbf{E}\times\mathbf{B} \text{ , PFR}} = 2\pi R n_0 \frac{\Phi_0}{\lambda_\Phi}\left(\frac{1}{\lambda_n} + \frac{1}{\lambda_\Phi}\right)^{-1}. \qquad (4)$$

Further assuming that $\lambda_\Phi << \lambda_n$ this becomes:

$$\Gamma_{\mathbf{E}\times\mathbf{B} \text{ , PFR}} = 2\pi R n_0 \Phi_0. \qquad (5)$$

The integrated particle flux towards the HFS is linearly proportional to the product of density and plasma potential in the common SOL right below the X-point and independent of the actual decay length of λ_Φ as long as $\lambda_n >> \lambda_\Phi$. This means that the radial gradient from the data does not need to be solved to calculate the integrated poloidal flux in the PFR as long as $\lambda_n >> \lambda_\Phi$, which is corroborated by the DTS data.

Using equations 2 and 5 and the DTS measurements, it is observed that in attached conditions, the plasma potential in the divertor leg below the X-point is higher than 100 V and results into a strong $\Gamma_{\mathbf{E}\times\mathbf{B} \text{ , PFR}}$ of the order of $1-2\times10^{22}$ /s towards the HFS divertor. This is a significant fraction of the order of 50% of the total integrated particle flux deposited on the LFS divertor plate in these conditions, peaking at 3×10^{22} /s for the highest density attached data point. As the plasma density is increased and the LFS target temperature collapse to ~ 1 eV, the plasma potential in the divertor leg below the X-point also collapses from 100 V down to a few V (Fig. 3a). As a result, the $\Gamma_{\mathbf{E}\times\mathbf{B} \text{ , PFR}}$ is reduced down to below 5×10^{21} /s.

These observations are qualitatively consistent with UEDGE predictions including cross-field drifts (Fig. 3b). The simulations indicate that as long as the LFS target remains attached, the plasma potential near the separatrix below the X-point remains above 50 V, driving a strong $\Gamma_{\mathbf{E}\times\mathbf{B} \text{ , PFR}}$ of the order of $0.8-1.5\times10^{22}$ /s towards the HFS divertor. As the plasma enters into detached conditions, the potential in the SOL below the X-point collapses to a few eV and the $\Gamma_{\mathbf{E}\times\mathbf{B} \text{ , PFR}}$ flux is diminished. As a result, the simulated target conditions evolve into a strongly detached, high density divertor conditions.
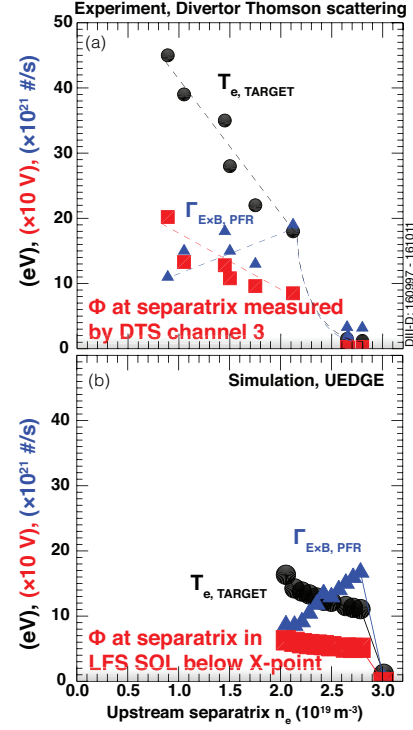

FIG. 3. (a) Measured LFS target electron temperature (black circles), inferred plasma potential at the LFS divertor leg separatrix at the DTS channel 3 level (Fig. 1) (red squares), and calculated $\mathbf{E}\times\mathbf{B}$-drift flux from LFS to HFS. (b) Simulated LFS target electron temperature (black circles), plasma potential at the LFS divertor leg separatrix below the X-point (red squares), and $\mathbf{E}\times\mathbf{B}$-drift flux from LFS to HFS.

Even though both divertor legs are strongly detached in the detached UEDGE cases in this study, the potential profile in the divertor is not completely flat in the simulations. In the common SOL, the simulation predicts flat potential profiles consistent with the experimental estimate. However, in the PFR, the simulations predict formation of a potential hill with peak potentials of the order of 50 – 100 V below the X-point. This hill is formed entirely by the current term in the equation (1), which was neglected in the previous analysis. The vertical ∇B-drift drives charge separation and vertical current. In the vicinity of the X-point, this drives a vertical current across the separatrix from the confined plasma to the common SOL and from the common SOL to the PFR. To maintain current continuity, these cross-field currents lead to parallel return currents along the field lines (Pfirsch-Schlüter currents) [24, and references therein]. In the PFR, these parallel currents propagate towards the target plates. Once both divertor legs are detached, T_e in the PFR is reduced down to a 1 – 2 eV, reducing the parallel electrical conductivity down to 1.5 – 4×10^3 Ω^{-1}m^{-1}. For $j_\parallel$ of the order of 3×10^4 A/m^2, as measured by the Langmuir Probes and predicted by

UEDGE in the LFS PFR in detached conditions, the parallel potential gradient is calculated to be of the order of 7 – 20 V/m. This procedure generates a potential hill in the private flux region, as is observed in the simulations. In the simulations this drives a self-closing counter clockwise circulating $\mathbf{E} \times \mathbf{B}$-vortex, such that the net $\mathbf{E} \times \mathbf{B}$-flux between the divertor legs remains low, while the peak $\mathbf{E} \times \mathbf{B}$-flux densities in the PFR are of the order of $3 \times 10^{23}/\mathrm{m}^2\mathrm{s}$. However, since the net $\mathbf{E} \times \mathbf{B}$ particle flux remains low, this $\mathbf{E} \times \mathbf{B}$-vortex does not impact the in-out asymmetries between the divertor legs.

The UEDGE simulations indicate that while radial $\mathbf{E} \times \mathbf{B}$-drift is needed to transport particles to the region of strong poloidal $\mathbf{E} \times \mathbf{B}$-drift in the PFR, it is the poloidal $\mathbf{E} \times \mathbf{B}$-drift that is driving the strong particle sink in the LFS divertor. As the LFS divertor detaches, the total radial plasma flux from LFS common SOL to PFR in the simulations increases by a factor of 2.5, primarily due to the increased density. However, as the net poloidal $\mathbf{E} \times \mathbf{B}$-drift in the PFR from LFS to HFS is diminished, particle recycling on the LFS PFR target is increased. This increases the neutral return flux from the LFS PFR to the common SOL. In the attached conditions, only 10% of the ions crossing from the LFS common SOL to the PFR are predicted to remain in the LFS divertor and return as neutrals, whereas in the detached conditions this fraction is 90%.

The step-like transition from an attached state to a detached state could be caused by any transient density increase and temperature reduction in the divertor, such as the conditions following an ELM in an ELMy H-mode plasma. In plasmas with the $\mathbf{B} \times \nabla \mathrm{B}$-drift away from the active X-point (rev. $\mathbf{B}_\mathrm{T}$), the $\mathbf{E} \times \mathbf{B}$ drift circulation does provide a density increase in the LFS in attached conditions lowering target temperatures. As a result, the physics mechanism described in this letter does not lead to this type of step like detachment onset in the LFS divertor in rev. $\mathbf{B}_\mathrm{T}$ plasmas. This consistent with experimental measurements and simulations showing that in rev. $\mathbf{B}_\mathrm{T}$ in H-mode, steady LFS divertor conditions with peak T_e of 3 – 5 eV can be achieved (Fig. 4). A smooth transition from attached to detached conditions is also observed in low confinement mode (L-mode) plasmas in both field directions in DIII-D (Fig. 4a, only fwd. $\mathbf{B}_\mathrm{T}$ shown). This indicates that sufficiently strong electric potential gradients in the divertor, characteristic of H-mode operation, are required for the divertor solution to bifurcate into the attached and detached branches.

Controlling the state of divertor detachment is expected to be necessary to protect the divertor plates in the next step fusion devices. The reactor design activities typically target the minimum degree of detachment that satisfies the engineering limits of the plasma facing components to optimize plasma performance with adequate divertor heat flux mitigation and particle throughput with pumping. The work documented in this letter
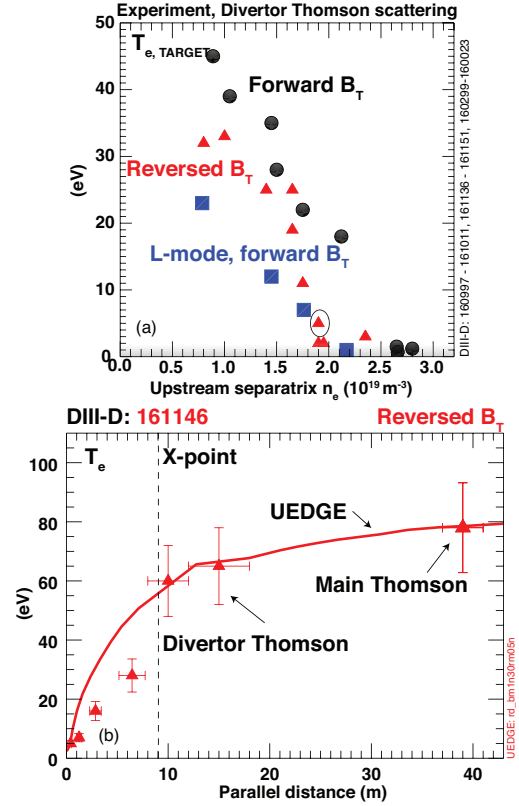

FIG. 4. (a) Measured electron temperature in front of the LFS divertor target in H-mode in fwd. $\mathbf{B}_\mathrm{T}$ (black circles), in rev. $\mathbf{B}_\mathrm{T}$ (red triangles), as well as in L-mode in fwd. $\mathbf{B}_\mathrm{T}$ (blue squares) as a function of measured upstream separatrix electron density. (b) Measured and simulated T_e profiles along a flux tube near the separatrix in the LFS SOL in rev. $\mathbf{B}_\mathrm{T}$ with peak target T_e in the range of 3 – 5 eV. The illustrated plasma is circled in Figure 4 a

indicates that the non-linear feedback between the state of divertor conditions and cross-field drifts can significantly modify the transition between attached and detached conditions. In the DIII-D plasmas investigated in this study, this non-linear feedback causes the operational window of partially detached divertor conditions to vanish as the divertor bifurcates between strongly attached and detached conditions. However, this does not mean that partially detached conditions cannot be achieved in the next step devices, since the non-linear behavior of the divertor plasmas is impacted by SOL power levels, spatial scales, divertor geometries, divertor densities, and plasma impurity composition, all of which are projected to be quite different in reactor scale devices when compared to these DIII-D plasmas. The implication of the work is that the detachment transition can be impacted substantially by the non-linear cross-field drift feedback and the modern divertor design studies should aim to include analysis with cross-field drifts to evaluate the magnitude of these effects.

* jarvinena@fusion.gat.com
† General Atomics, San Diego, California 92186-5608, USA
‡ Aalto University, Otakaari 1, Espoo, Finland
§ Oak Ridge Associated Universities, Oak Ridge, Tennessee, USA

[1] S. Itoh and K. Itoh, Phys. Rev. Lett. **60**, 2276 (1988).
[2] F. Wagner, Plasma Phys. Cont. Fusion **49**, B1 (2007).
[3] A. Loarte *et al.*, Phys. Rev. Lett. **83**, 3657 (1999).
[4] A. Loarte *et al.*, Nucl. Fusion **47**, S203 (2007).
[5] A. Kallenbach *et al.*, Plasma Phys. Control. Fusion **55**, 124041 (2013).
[6] D. Post *et al.*, Phys. Plasmas **2**, 2328 (1995).
[7] B. Lipschultz *et al.*, Nucl. Fusion **56**, 056007 (2016).
[8] I. Hutchinson, Nucl. Fusion **34**, 1337 (1994).
[9] A. Kallenbach *et al.*, Nucl. Fusion **55**, 053026 (2015).
[10] B. Lipschultz *et al.*, Fus. Sci. Tech. **51**, 369 (2007).
[11] C. Giroud *et al.*, Plasma Phys. Control. Fusion **57**, 035004 (2015).
[12] N. Asakura *et al.*, J. Nucl. Mat. **266-269**, 182 (1999).
[13] T. N. Carlstrom *et al.*, Rev. Sci. Instrum. **68**, 1195 (1997).
[14] A. G. McLean *et al.*, J. Nucl. Mat. **463**, 533 (2015).
[15] D. Eldon *et al.*, Nucl. Fusion **57**, 066039 (2017).
[16] T. D. Rognlien *et al.*, Phys. Plasmas **6**, 1851 (1999).
[17] W. Eckstein, J. Nucl. Mat. **248**, 1 (1997).
[18] J. Davis and A. Haasz, J. Nucl. Mat. **241-243**, 37 (1997).
[19] P. C. Stangeby *et al.*, Nucl. Mat. Ene. **12**, 876 (2017).
[20] J. Boedo *et al.*, Phys. Plasmas **7**, 1075 (2000).
[21] A. G. McLean *et al.*, Phys. Plasmas (Submitted 2017).
[22] P. C. Stangeby, The Plasma Boundary of Magnetic Fusion Devices , Taylor & Francis (2000).
[23] S. I. Braginskii, Transport Processes in a Plasma, Reviews of Plasma Physics , 205.
[24] M. J. Schaffer *et al.*, Nucl. Fusion **37**, 83 (1997).